





Asymmetric Transport of the Earth's Polar Outflows by the Interplanetary Magnetic Field

Juan Wang^{1,2,3} , Can Huang¹, Yasong S. Ge¹, Aimin Du¹, Xueshang Feng^{4,5} , and Kun Li⁶

¹ Key Laboratory of Earth and Planetary Physics, Institute of Geology and Geophysics, Chinese Academy of Sciences, Beijing, People's Republic of China
huangcan@mail.iggcas.ac.cn

² School of Systems Science, Beijing Normal University, Beijing, People's Republic of China

³ State Key Laboratory for Space Weather, Chinese Academy of Sciences, Beijing, People's Republic of China

⁴ SIGMA Weather Group, State Key Laboratory for Space Weather, National Space Science Center, Chinese Academy of Sciences, Beijing, People's Republic of China

⁵ Laboratory for Space Weather Storms, Institute of Space Science and Applied Technology, Harbin Institute of Technology, Shenzhen, People's Republic of China

⁶ School of Atmospheric Sciences, Sun Yat-Sen University, Zhuhai, People's Republic of China

Received 2019 April 19; revised 2019 August 2; accepted 2019 August 4; published 2019 August 20

Abstract

The polar outflows, as an important plasma source of the Earth's magnetosphere, usually exhibit significant north–south asymmetries, which can strongly affect the plasma distributions in the magnetotail lobe and perhaps contribute to the substorm triggering. But the mechanism of the asymmetric transport of these outflows is still unclear. In this Letter, 3D global magnetohydrodynamic (MHD) simulations are performed to investigate the development of the polar outflows after their escapes from the inner boundary under influences of the interplanetary magnetic field (IMF) B_x . It is found that the velocity of northern polar outflows is much stronger than the south. We suggest that the IMF B_x causes the north–south asymmetries in the magnetospheric configuration, and subsequently, great differences of the force and mass distributions appear between the two hemispheres, which lead to the significant north–south asymmetries in the transport of the polar outflows. We also discuss the differences in the acceleration mechanisms of the polar outflows between the northward and southward IMF cases.

Key words: Earth – magnetic fields – magnetohydrodynamics (MHD) – plasmas – solar–terrestrial relations – solar wind

1. Introduction

The polar outflows are essentially outward flows traveling along the local magnetic field lines, from the high-latitude polar caps to the magnetosphere (Moore et al. 1997). Over the past 50 yr, satellite observations have further verified the existence of the polar outflows and cataloged their primary features (Banks & Holzer 1969; Chappell et al. 1987; Abe et al. 2004; Lavraud et al. 2005; Zhang et al. 2016). The outflows are observed ranging from thousands of kilometers to several Earth radii (Yau et al. 2007) and are mainly composed of O^+ , He^+ , H^+ ions and electrons. The ion population changes with the solar cycle, dominated by O^+ ions up to thousands of kilometers.

The O^+ ions, relatively rare in the solar wind, are found to be ubiquitous in the magnetosphere (Shelley et al. 1972), indicating that polar outflow is a significant contributor to the plasma population of the magnetosphere (Yau & André 1997; Yau et al. 2007). For decades, the quantitative contribution of the polar outflow flux to the magnetosphere has attracted many researchers' interest (Yau & André 1997; Chappell et al. 2000), and it is regarded to determine the density and velocity of the inner boundary (about 2 ~ 3 Earth radii) of the magnetohydrodynamic (MHD) models for the magnetosphere. The state-of-the-art ionospheric outflow models are the generalized polar wind (GPW) model (Barakat & Schunk 2006), the Polar Wind Outflow Model (PWOM; Glocer et al. 2009), and the 1D ionosphere–polar wind model (Varney et al. 2014). Recent studies have found that the polar outflows are highly associated with the ring current, playing an important role in both magnetosphere–ionosphere coupling and magnetospheric dynamics (Chappell et al. 1987;

Moore et al. 1997; Engwall et al. 2009). Besides, it is also found to be a contributor of the injected plasma in the magnetotail, creating auroras, substorms, and storms (Moore et al. 1997; Haaland et al. 2017).

As directly related to the mass injections to the magnetosphere, the transport process of the polar outflows is critical. It has been widely studied since the early reports of the polar outflows in the 1960s (e.g., Banks & Holzer 1968; Nagai et al. 1984; Su et al. 1998; Yau et al. 2007). Using a simplified hydrodynamic model, which only included the quasi-steady assumption and the momentum equations in a proton–electron system, Banks & Holzer (1968) suggested the polar outflows are supersonic. The velocity and density profiles predicted that the protons flow along the magnetic field lines at supersonic speeds above the H^+O^+ collision region due to the presence of the ambipolar electric field. Nagai et al. (1984) confirmed this view at the high-altitude region. Su et al. (1998) presented a more comprehensive study of the observed characters of polar outflows based on POLAR, mostly near its apogee (about 50,500 km) and perigee (about 5000 km). They found that the bulk velocity of the polar outflows increases with altitude. Yau et al. (2007) observed that the polar outflow velocity increases with altitude, which is strongly correlated with the electron temperature. The increase rate at low altitude is larger at solar minimum than at solar maximum. At the high altitude, the reverse is the case. They proposed that the acceleration process of the dominant polar wind ions may be different at low and high altitudes.

A recent simulation performed by Barakat et al. (2015) showed that the southern hemisphere has generally higher outflow fluxes than the northern hemisphere, and the authors attributed the north–south asymmetries to the differences in the

geographic–geomagnetic pole offset between the two hemispheres. Moreover, the north–south asymmetries of the polar outflows may affect the plasma distribution in the magnetotail lobes. Haaland et al. (2017) observed a north–south asymmetry in the cold plasma density of the tail lobes, with consistently more ions in the northern lobe. They suggested that the periodical variations of the Earth’s tilt angle can result in such asymmetries through the asymmetric ionization of two hemispheres. However, there is no direct observational evidence of the asymmetries of the polar outflows in the cusp regions. Moreover, due to the limitation of the satellite orbits, it is also difficult to make a quantitative assessment of the asymmetries based on the observation data.

In this Letter, we propose a new mechanism that causes north–south asymmetric transport of the polar outflows by 3D global MHD simulations (Wang et al. 2015, 2018). The interplanetary magnetic field (IMF) B_x brings about great differences in the polar outflows in high-altitude regions (from $3.5R_E$ to $10R_E$, where R_E is the Earth’s radius) between the northern and southern hemispheres. It is found that the IMF orientation can cause great differences in the configuration of the magnetosphere between the two hemispheres, and as a result, significant asymmetries in the polar outflows exist. Even the pole offset is absent in the simulations, we still find the north–south asymmetries in the polar outflows, and they are purely related to the IMF direction in this study. This Letter is organized as follows. We start with a description of the simulation model. Then, the simulation results are presented. At last, conclusions and discussions are made.

2. Simulation Model

The computational domain $3R_E \leq r < 156R_E$ is used here on a six-component grid system, which has been refined by the adaptive mesh refinement (AMR) method. The greatest grid resolutions near the bow shock and magnetopause are $0.2R_E$ and $0.12R_E$, respectively. In the AMR-CESE-MHD model, a two-dimensional ionospheric shell is placed at $r = 1.017R_E$, which is coupled with the inner boundary ($r = 3R_E$) self-consistently (Wang et al. 2015). The field-aligned current and electric field are mapped between the model’s inner boundary and the ionosphere along the dipole magnetic field lines, which establishes the magnetosphere–ionosphere coupling (Raeder et al. 1998). At the inner boundary, the Dirichlet condition is applied for the normal component of the time-dependent derived part of the magnetic field and the Neumann condition for its tangential components (Tanaka 1994). At the inner boundary, the plasma density is fixed to be 25 cm^{-3} , and the thermal pressure is determined by the Neumann condition. The radial component of the bulk velocity is set to be zero, and its tangential component is calculated by the magnetosphere–ionosphere coupling. At the outer boundary ($r = 156R_E$), a fixed inflow boundary condition and a free outflow boundary condition are used at the dayside and nightside, respectively. The x and z components of the IMF are set to be 30 nT and ± 5 nT, and the solar wind velocity along the Sun–Earth line is set to be -400 km s^{-1} during the simulation. The plasma number density and the temperature of the solar wind are 5 cm^{-3} and $2.32 \times 10^5 \text{ K}$. More details about this model can be found in the previous works (e.g., Wang et al. 2014, 2015).

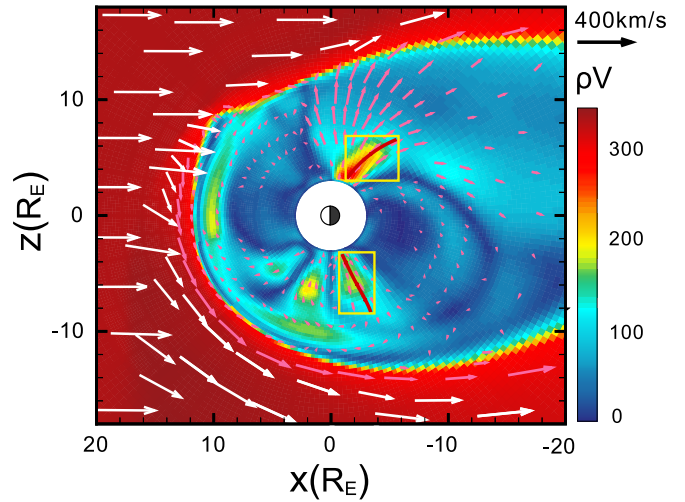


Figure 1. Overview of the north–south asymmetric transport of the polar outflows during a typical northward IMF condition, under the influences of a B_x component. The white (pink) arrows are the representation of the flows outside (inside) the magnetopause. The length of the arrows denotes the velocity magnitude. In contrast, the length of the arrow in the left-most part of the figure (in the solar wind) denotes 400 km s^{-1} . The background colors represent the plasma flux in the noon–midnight plane.

3. Results

Figure 1 shows the spatial distributions of the flow vectors in the noon–midnight meridian plane during northward IMF with a B_x component. The data are obtained at the time $t \approx 7.79$ hr when the simulation reaches a nearly steady state with no obvious changes of the dynamic variables within a half hour. The white (pink) arrows represent the flows outside (inside) of the magnetopause. The background colors represent the plasma flux ρV , where ρ and V are the number density and bulk velocity of plasma, respectively. The regions marked with yellow boxes are the interested regions (with an approximate range $3.5R_E < r < 10R_E$) of this study. There are polar outflows escaping from the polar cap and flowing into the magnetotail both in the northern and southern cusp regions. The northern outflow has a higher speed and flux, while the southern outflow has a lower speed and flux. That is to say, significant north–south asymmetric transport of the polar outflows is present in the high-altitude cusp regions. From the flow vectors, it is clear that the polar outflows in both hemispheres get accelerated after leaving the inner boundary. The acceleration in the north is more obvious, and the peak velocity of the northern polar outflow is much greater. Recent observations show that these regions are filled with supersonic or subsonic ionospheric outflows traveling along local magnetic field lines (Moore et al. 1997), and these polar outflows are important plasma sources of the magnetosphere (Shelley et al. 1972; Yau & André 1997; Yau et al. 2007). The polar plasma outflows accelerate continually into the magnetotail lobe, and even into the near-Earth plasma sheet (Cladis 1986).

The enlarged views of the polar cusp regions in Figure 1 can help us to understand the details of the acceleration progress of the polar outflows. Two specified streamlines are traced along the ridge lines of the flux in northern and southern cusp regions (colored in red in Figure 1). The blue solid lines in the top and bottom panels of Figure 2 present the outflow velocities along the specified streamlines in the northern and southern hemispheres, respectively. The velocity of the northern polar outflow increases to be about 116 km s^{-1} , while that of the southern polar outflow peaks at about 45 km s^{-1} . Consistent

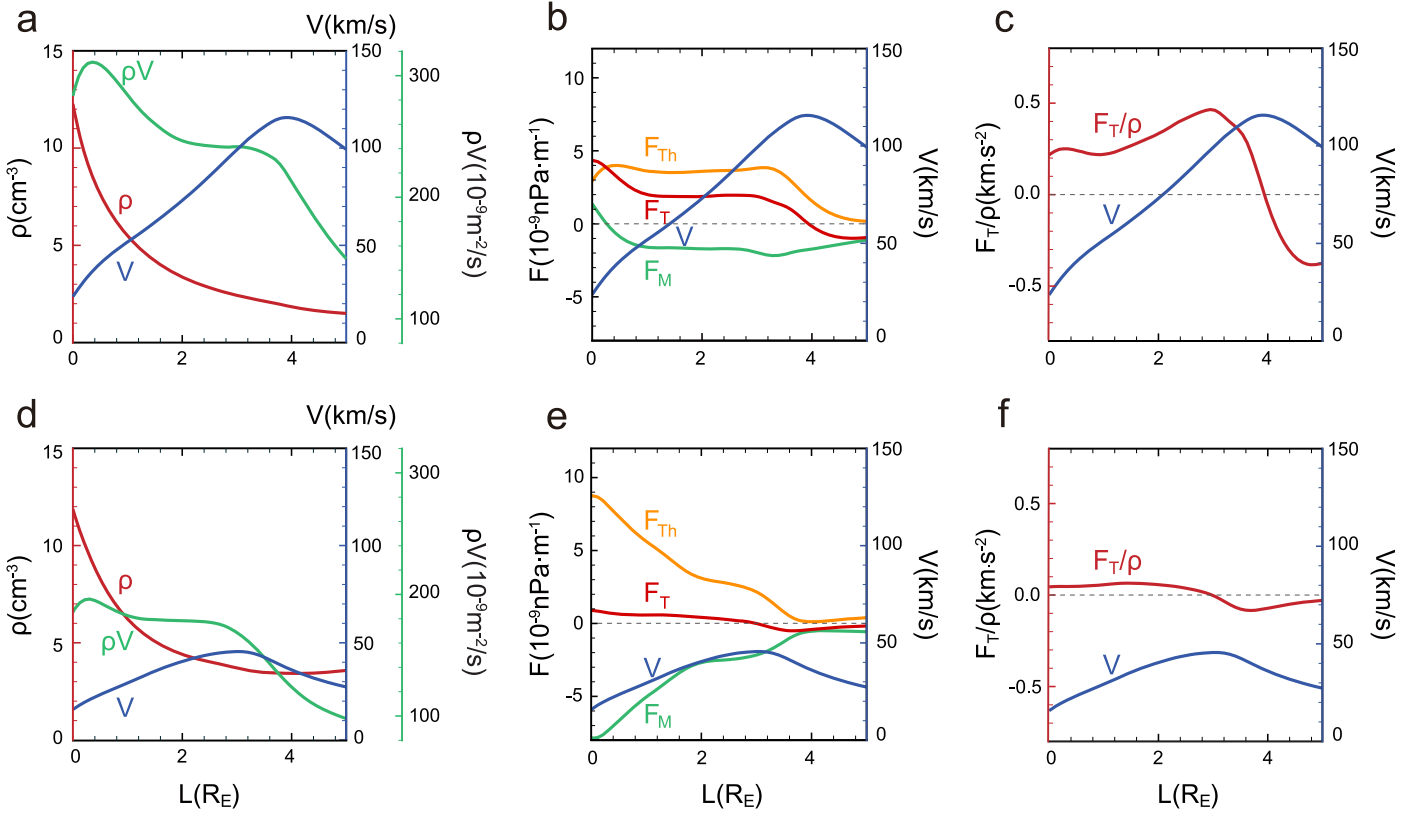


Figure 2. Profiles of the plasma density, velocity, forces, and acceleration speed along the specified streamlines (marked with red lines in Figure 1) in the northern (top panels) and southern (bottom panels) cusp regions. L denotes the distance along the specified streamline measured from $r = 3.5R_E$. In (a) and (d), the red, blue, and green lines represent ρ , V , and ρV . The orange, green, and red lines denote the thermal pressure force, Ampère force, and total force in (b) and (e). The red lines in (c) and (f) show the acceleration speed.

with Figure 1, the velocity of the northern polar outflow is much higher than that of the southern outflow. Both outflows accelerate first, and then decelerate. But the deceleration phase in the south is much earlier. As shown by the red lines in Figures 2(a) and (d), the plasma densities in the north and south along the streamlines both continue decaying. The number density in the southern hemisphere is higher than that in the northern hemisphere after the polar plasma flows out from the inner boundary. The plasma flux ρV is more suitable for the investigation on the transport of the polar outflows. As the green lines in Figures 2(a) and (d) show, the flux in the north is significantly larger than that in the south. It means there is more plasma injecting to the northern tail due to the asymmetric transport of the polar outflows. Comparing the flux with the density and velocity, it is clear that the more effective acceleration of the polar outflows in the northern cusp results in the higher plasma flux in the north.

In order to find the formation mechanism of the north–south asymmetries in the acceleration of the polar outflows, the distributions of the forces acting on the polar outflows should be shown along the streamlines. From the continuity and momentum equations, we can obtain $\rho \partial \mathbf{u} / \partial t + (\rho \mathbf{u} \cdot \nabla) \mathbf{u} = -\nabla p + \mathbf{J} \times \mathbf{B}$, where \mathbf{B} , \mathbf{u} , ρ , and p denote the magnetic field, plasma velocity, density, and thermal pressure, respectively. Here, the current density is obtained by $\mathbf{J} = \nabla \times \mathbf{B} / \mu_0$. The acceleration of the polar outflow plasma is mainly determined by the thermal pressure gradient force and the Ampère force. Figures 2(b) and (e) present these two forces acting on the polar outflows along the specified streamlines in the northern and southern hemispheres, respectively. In the north, the thermal

pressure gradient force (orange) keeps positive, while the Ampère force (green) turns to be negative at $L \approx 0.3R_E$. Here, L denotes the distance along the specified streamline measured from the point $r = 3.5R_E$ (the fixed inner boundary for density is located at $r = 3R_E$, so there are some differences between the left ends of the plots of densities shown in Figures 2(a) and (d)). The thermal pressure gradient force acting on the southern polar outflow along the specified streamline is also positive all the way, while the Ampère force keeps negative. As a result, the total force (the red lines in Figures 2(b) and (e)) acting on the northern polar outflow along the specified streamline remains positive when $L < 4R_E$, while in the southern hemisphere, the total force turns negative at $L \approx 3R_E$. We suggest that the polar plasmas are pumped out from the inner boundary by the thermal pressure gradient force, and then expand upward along the open magnetic field lines. The Ampère force drives the polar outflows to accelerate outward from the inner boundary in the northern hemisphere, but suppresses them to accelerate when they are near the flank magnetopause.

Considering that the acceleration speed is also sensitive to the density, Figures 2(c) and (f) plot the acceleration speeds (red) and the velocities (blue) of the northern and southern polar outflows along the specified streamlines. It is worth noting that the spatial variation of the flow velocity can present the time variation of the flow velocity in the fluid frame when the simulation reaches a quasi-steady state ($\partial/\partial t \approx 0$). That is to say, the acceleration speed can be represented by the spatial variation of the outflow velocity along a streamline. The slopes of the blue solid lines (the outflow velocity) are consistent with

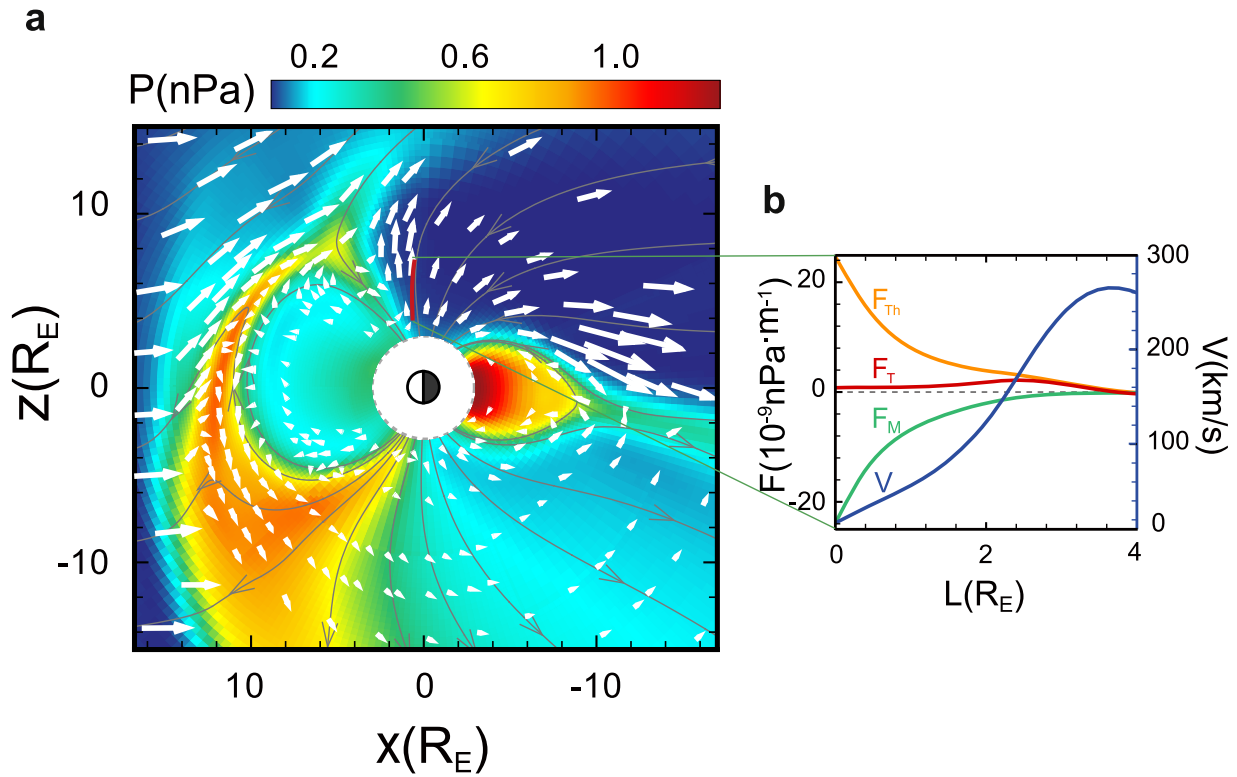


Figure 3. (a) Overview of the north–south asymmetric polar outflows during a typical southward IMF condition, under the influences of a B_x component. The gray lines are the magnetic field lines, the white arrows denote the flow vectors, and the red line denotes the specified streamline. The background colors represent the thermal pressure in the noon–midnight meridional plane. (b) The forces acting on the polar outflows along the specified streamline. The orange, green, and red lines denote the thermal pressure gradient, Ampère, and total forces along the streamline, respectively. The blue line represents the velocity.

the red solid lines (the acceleration speed) in Figures 2(c) and (f). We have also calculated $\rho V \partial V / \partial L$ (an approximation of $(\rho dV/dt)_L$ during the quasi-steady state), and found the curves of $\rho V \partial V / \partial L$ coincide with the total forces. From Figures 2(b) and (e), it can be found that the total force acting on the southern polar outflow is smaller than that acting on the northern polar outflow during the acceleration. The plasma density of the south is higher than that of the north as shown by Figures 2(a) and (d). Thus, the acceleration speed of the northern polar outflow is much higher. Moreover, the duration of the acceleration process in the north is longer than that in the south (see Figures 2(c) and (f)). Therefore, the acceleration of the northern polar outflow is much more effective.

We have also performed another similar simulation of the polar outflows during southward IMF with the same B_x component. The data are obtained at the time $t \approx 7.79$ hr when the simulation reaches a quasi-steady state. In Figure 3(a), the gray lines are the magnetic field lines, the white arrows are the flow vectors, and the red line is the specified streamline in the northern cusp region. Comparing to the pure southward IMF case (Ridley et al. 2010), the subsolar magnetic reconnection shifts northward and occurs in the high-latitude cusp region with the existence of the IMF B_x . The newly formed field lines transport tailward at the nightside or southward at the dayside. The tailward flux piles up in the tail lobes and another magnetic reconnection occurs in the tail, which is located in the southern hemisphere due to the influence of IMF B_x . The global image of the magnetosphere under such an IMF condition is similar to that under pure southward IMF, except that the whole magnetosphere rotates clockwise. Moreover, the polar outflow becomes almost invisible in the southern hemisphere, but it is still obvious

in the north. Figure 3(b) shows the forces acting on the polar outflows along the specified streamline in Figure 3(a). The orange, green, and red lines represent the thermal pressure gradient, Ampère, and total forces along the streamline, respectively. The velocity of the outflows keeps rising after they flow out from the inner boundary and before they reach $L = 3.6R_E$. The polar outflows speed up under the action of the thermal pressure gradient force, which is similar to the acceleration mechanism of the solar wind. Unlike the northward IMF case, in this case, the Ampère force plays as a dragging force, different from the thermal pressure, and prevents the polar plasma moving away from the inner boundary. However, the thermal pressure gradient force exceeds the Ampère force and dominates the direction of the acceleration of the polar outflows.

4. Conclusions and Discussions

In summary, global MHD simulations are performed to investigate the transport of the polar outflows after they escape from the inner boundary, with the existence of IMF B_x . There are great differences in the transport process of the polar outflows between the northern and southern hemispheres. In both the northward and southward IMF cases, the bulk velocities and plasma fluxes of the northern polar outflows are more obvious than those of the south. After diagnosis on the momentum equation of the magnetohydrodynamic fluid, it is found that the acceleration of the polar outflows is mainly determined by the thermal pressure gradient force and the Ampère force. The thermal pressure gradient force remains positive, driving the plasma to flow out from the inner boundary. The Ampère force mainly plays a negative role on

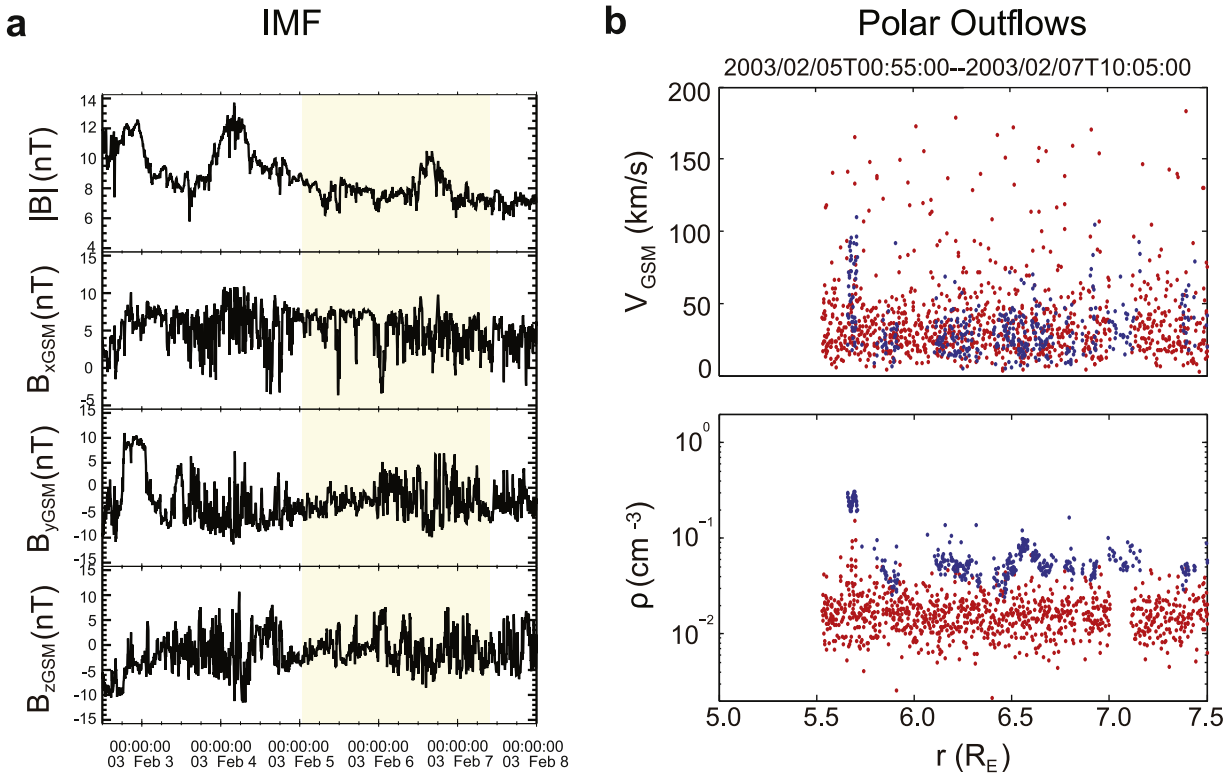


Figure 4. Cluster observations of the polar outflows in the cusp regions with the continuously positive IMF B_x . (a) The total and three components of the IMF (in 4 minute resolution) measured by the MAG instrument on board ACE. (b) The velocity and number density of the ions (in 4 s resolution) measured by the CIS instrument on board Cluster. The yellow regions in (a) show the time interval during which the Cluster spacecraft passed through the cusp regions, and the data points are plotted in (b).

the acceleration of the polar outflow under the northward (or southward) IMF. The positive total force acting on the polar outflows in the northern cusp is larger than that in the south, which causes the higher plasma flux in the northern cusp, though the density is lower.

Previous studies claimed that the polar outflows have significant influences on the global configuration of the magnetosphere (e.g., Brambles et al. 2010; Wiltberger et al. 2010; Welling & Zaharia 2012). The studies in this Letter propose that the IMF B_x component can cause north–south asymmetric magnetospheric configuration, leading to great differences in the polar outflows between the northern and southern hemispheres. It is inferred that the north–south asymmetries in the polar outflows are a probable explanation for the north–south asymmetries in the cold plasma density of the magnetotail lobes observed by satellites (Haaland et al. 2017). As far as is known, during southward IMF, magnetic reconnections occur at the subsolar magnetopause and the magnetotail in an open magnetosphere, while during northward IMF, magnetic reconnections can take place in the nightside of the cusps in a nearly closed magnetosphere (Dungey 1961). However, our simulations indicate that a northward IMF with a B_x component can generate a distorted magnetopause shape (not shown here). It is very fascinating that the magnetospheric configuration during such an IMF condition is somewhat similar to that during the southward IMF after some clockwise twisting. That is to say, the B_x component under northward IMF brings similar influences on the magnetosphere as the B_z component under southward IMF. We will make a further quantitative comparison in future work.

We have also analyzed the in situ observation data when the Cluster spacecraft passed through the northern and southern cusp regions. Figure 4(a) shows the IMF (in 4 minute resolution) measured by the MAG instrument (Smith et al. 1998) on board ACE from 2003 February 2, 1200 UT to 2003 February 8, 0000 UT when the B_x component of the IMF is almost positive. Figure 4(b) gives the velocity and number density of the ions (in 4 s resolution), which are measured by the CIS instrument (Rème et al. 2001) on board Cluster, from 0055 UT February 5 to 1005 UT February 7, 2003. During the time interval, Cluster passed through the northern and southern cusp regions once. The data shown in the figure are chosen by these criteria: (1) the magnetic latitudes of the satellite orbit are larger than 50° , (2) there is no obvious difference in the number of data points between the northern and southern cusp regions, (3) the altitudes of the satellite orbit range from $4R_E$ to $7R_E$ in the cusp regions (the main acceleration area of the polar outflows in Figure 2), and (4) the ions flow upward and satisfy $\mathbf{z} \cdot (\mathbf{V} \cdot \mathbf{B}) < 0$ (also used in Li et al. 2012, and here the magnetic fields are obtained from the FGM, Balogh et al. 2001, instrument). These conditions ensure that the focused regions are more similar to those in our simulations. In this Letter, the geocentric solar magnetospheric (GSM) coordinate system is used for the observations. The red and blue dots in Figure 4(b) are collected from the northern and southern hemispheres, respectively. There are much more data points with high velocities ($>100 \text{ km s}^{-1}$) in the north than the south, and the densities in the north are mostly lower than those in the south. These are consistent with the simulation results discussed above. It should be noted that it is difficult to trace the polar outflow along a specified streamline by the observation data,

which leads to that we cannot investigate the acceleration mechanism of the polar outflows only using the observation data. In any case, Figure 4 tells us that north–south asymmetries do exist in the polar outflows in the cusp regions between $r = 5.5R_E$ and $r = 7.5R_E$ with the presence of the IMF B_x component.

We have only exhibited the simulation results with a positive IMF B_x in this Letter. According to the symmetrical principle of the MHD equations, it can be predicted that opposite conclusions maybe obtained if the IMF B_x is set to be negative. Besides, the geographic–geomagnetic pole offset, which is removed in our study, can also introduce some asymmetries of the polar outflows (Barakat et al. 2015). The asymmetric transport of the polar outflows shown in our results can cause the asymmetric plasma injections in tail, and the ion density of which hemisphere is higher depends on the orientation of the IMF B_x . The observation results from Barakat et al. (2015) and Haaland et al. (2017) are not incompatible with our results. It is necessary in further research that the observation data are classified by the real-time IMFs and then analyzed statistically.

The magnitude of the IMF B_x used in this Letter is a few times larger than a typical value in the near-Earth space. So extra runs with IMF $B_x = 15$ nT and $B_z = \pm 5$ nT have also been performed. The symmetries still exist with the decrease of B_x , except the velocity of the southern polar outflow increases a little and the asymmetries become weaker. All these diagnoses of the polar outflows in this study are limited to the cusp regions between $r = 3.5R_E$ and $r = 10R_E$. Our results have not involved the further acceleration process of the polar outflows in a more distant region. Besides, for simplicity, the geographic–geomagnetic pole offset has not been included in the simulations, and its synergistic effect with solar wind is our future work. Actually, polar outflows have also been observed on other planetary bodies in the solar system, such as Titan (Edberg et al. 2011), Mars (Collinson et al. 2015), and Saturn (Felici et al. 2016). The results in this Letter may be available to reference for the research of the polar outflows on these planetary bodies.

We thank Andrew W. Yau for the valuable suggestions. This research was supported by the National Natural Science Foundation of China (grants 41604144, 41531073, 41474144, 41674168, 41774176, and 41704164), and the China Post-doctoral Science Foundation (2018M630198). The work was also supported by the Specialized Research Fund for State Key Laboratories. The simulations were carried out on the

computational facilities in the Computer Simulation Lab of IGGCAS, and the data can be obtained by contacting Juan Wang through e-mail (juanwang@mail.iggcas.ac.cn). We thank the MAG instrument team and the ACE Science Center for providing the ACE data. The observation data of the *Cluster* measurements are available from the *Cluster* Science Archive (<https://cosmos.esa.int/web/csa>). We thank the FGM, CIS instrument teams.

ORCID iDs

Juan Wang  <https://orcid.org/0000-0003-1234-3150>
Xueshang Feng  <https://orcid.org/0000-0001-8605-2159>

References

- Abe, T., Yau, A. W., Watanabe, S., et al. 2004, *JGRA*, 109, A09035
 Balogh, A., Carr, C. M., Acuna, M. H., et al. 2001, *AnGeo*, 19, 1207
 Banks, P. M., & Holzer, T. E. 1968, *JGRA*, 73, 6846
 Banks, P. M., & Holzer, T. E. 1969, *JGRA*, 74, 6317
 Barakat, A. R., Eccles, J. V., & Schunk, R. W. 2015, *GeoRL*, 42, 8288
 Barakat, A. R., & Schunk, R. W. 2006, *JGRA*, 111, A12314
 Brambles, O. J., Lotko, W., Damiano, P. A., et al. 2010, *JGRA*, 115, A00J04
 Chappell, C. R., Giles, B. L., Moore, T. E., et al. 2000, *JASTP*, 62, 421
 Chappell, C. R., Moore, T. E., & Waite, J. H., Jr. 1987, *JGRA*, 92, 5896
 Cladis, J. B. 1986, *GeoRL*, 13, 893
 Collinson, G., Mitchell, D., Glocer, A., et al. 2015, *GeoRL*, 42, 9128
 Dungey, J. W. 1961, *PhRvL*, 6, 47
 Edberg, N. J. T., Agren, K., Wahlund, J. E., et al. 2011, *P&SS*, 59, 788
 Engwall, E., Eriksson, A. I., Cully, C. M., et al. 2009, *NatGe*, 2, 24
 Felici, M. C., Arridge, S., Coates, A. J., et al. 2016, *JGRA*, 121, 338
 Glocer, A., Toth, G., Gombosi, T., et al. 2009, *JGRA*, 114, A05216
 Haaland, S., Lybekk, B., Maes, L., et al. 2017, *JGRA*, 122, 136
 Lavraud, B., Fedorov, A., Budnik, E., et al. 2005, *JGRA*, 110, A02209
 Li, K., Haaland, S., Eriksson, A., et al. 2012, *GeoRL*, 39, L18102
 Moore, T. E., Chappell, C. R., Chandler, M. O., et al. 1997, *Sci*, 277, 349
 Nagai, T., Waite, J. H., Jr, Green, J. L., et al. 1984, *GeoRL*, 11, 669
 Raeder, J., Berchem, J., & Ashour-Abdalla, M. 1998, *JGRA*, 103, 14787
 Rème, H., Aoustin, C., Bosqued, J. M., et al. 2001, *AnGeo*, 19, 1303
 Ridley, A. J., Gombosi, T. I., Sokolov, I. V., et al. 2010, *AnGeo*, 28, 1589
 Shelley, E. G., Johnson, R. G., & Sharp, R. D. 1972, *JGRA*, 77, 6104
 Smith, C. W., L'Heureux, J., Ness, N. F., et al. 1998, *SSRV*, 86, 613
 Su, Y. J., Horwitz, J. L., Wilson, G. R., et al. 1998, *JGRA*, 103, 2279
 Tanaka, T. 1994, *JCoPh*, 111, 381
 Varney, R. H., Solomon, S. C., & Nicolls, M. J. 2014, *JGRA*, 119, 8660
 Wang, J., Du, A. M., Zhang, Y., et al. 2015, *ScChE*, 58, 1235
 Wang, J., Feng, X. S., Du, A. M., et al. 2014, *JGRA*, 119, 9919
 Wang, J., Guo, Z. F., Ge, Y. S., et al. 2018, *JWSWC*, 8, A41
 Welling, D. T., & Zaharia, S. G. 2012, *GeoRL*, 39, L23101
 Wiltberger, M., Lotko, W., Lyon, J. G., et al. 2010, *JGRA*, 115, A00J05
 Yau, A. W., Abe, T., & Peterson, W. K. 2007, *JASTP*, 69, 1936
 Yau, A. W., & André, M. 1997, *SSRV*, 80, 1
 Zhang, Q. H., Zong, Q. G., Lockwood, M., et al. 2016, *GeoRL*, 43, 1845